Materials design principles of ancient fish armour

BENJAMIN J. F. BRUET[1]*, JUHA SONG[1]*, MARY C. BOYCE[2] AND CHRISTINE ORTIZ[1]†

[1]Department of Materials Science and Engineering, Massachusetts Institute of Technology, 77 Massachusetts Avenue, Cambridge, Massachusetts 02139, USA
[2]Department of Mechanical Engineering, Massachusetts Institute of Technology, 77 Massachusetts Avenue, Cambridge, Massachusetts 02139, USA
*These authors contributed equally to this work
†e-mail: cortiz@mit.edu.

Published online: 27 July 2008; doi:10.1038/nmat2231

Knowledge of the structure–property–function relationships of dermal scales of armoured fish could enable pathways to improved bioinspired human body armour, and may provide clues to the evolutionary origins of mineralized tissues. Here, we present a multiscale experimental and computational approach that reveals the materials design principles present within individual ganoid scales from the 'living fossil' *Polypterus senegalus*. This fish belongs to the ancient family Polypteridae, which first appeared 96 million years ago during the Cretaceous period and still retains many of their characteristics. The mechanistic origins of penetration resistance (approximating a biting attack) were investigated and found to include the juxtaposition of multiple distinct reinforcing composite layers that each undergo their own unique deformation mechanisms, a unique spatial functional form of mechanical properties with regions of differing levels of gradation within and between material layers, and layers with an undetectable gradation, load-dependent effective material properties, circumferential surface cracking, orthogonal microcracking in laminated sublayers and geometrically corrugated junctions between layers.

Dermal armour in fish first appeared at the beginning of the Paleozoic period during the Ordovician with the rise of the Ostracoderms ~500 Myr ago[1] and was common among these earliest fishes[2]. In 1857, the geologist Hugh Miller speculated on the mechanical design of ganoid scales by drawing analogies with 'the principle of the two tables and diploe of the human skull, the principle of the variously arranged coats of the human stomach, and the principle of Oliver Cromwell's fluted pot.'[3]. Romer in 1933 hypothesized that dermal armour served as a protection from predators[4] and subsequently a number of additional mechanical and non-mechanical functions have been proposed[5–7]. As ancient fish became more predaceous[8], their armour evolved in terms of their multilayered material structures and overall geometries; for example, larger plates broke up into many smaller ones, the thickness of various layers decreased, and the number of layers decreased, all of which would have decreased weight, improved flexibility and manoeuvrability and increased speed[2]. Interestingly, many parallels can be found between the evolution of armour in the animal world and human-designed engineered body armour, both of which seem to be controlled by a balance between protection and mobility, to maximize survivability[9]. The design strategies used by mineralized biological tissues, in general, are an area of great interest and much progress has been made in the understanding of concepts such as crystalline nucleation, growth and morphology, biomacromolecular intercalation and reinforcement, modulation of crystal texture, stabilization of amorphous phases, small length scale effects, heterogeneity and so on[10–16]. However, little is known about the mechanical properties of individual dermal armour plates and scales. For example, the mechanical roles of the mathematical form of material property variations (such as gradients) both within and between various layers, the number of layers, the layer and junction thicknesses, structures and geometries, the constitutive laws of each layer and so on, and more importantly the relationship of these parameters to larger scale biomechanical performance and environmental stresses (such as predatory or territorial attacks). Here, we use a multiscale experimental and computational approach, developed from our previous works[15,17], to elucidate such design principles, in particular with regards to multilayering and grading. The general methodologies presented here are applicable to a broad range of multilayered protective exoskeletal materials (for example crustacean[18], insect[19] and gastropod mollusc[10]) and able to yield a mechanistic understanding of how different organisms were designed, and possibly evolved, to sustain the loads they experience in their environment. Such fundamental knowledge, in particular threat–design relationships, holds great potential for the development of improved biologically inspired structural materials[20], for example soldier, first responder and military vehicle armour applications[9].

In this report, we focus on a fascinating model system, the interlocking, quad-layered, mineralized scales from *Polypterus senegalus*, which belongs to the fish family Polypteridae (appearing ~96 Myr ago in the Cretaceous period[21]), and still lives today, primarily at the bottoms of freshwater, muddy shallows and estuaries in Africa[22]. *P. senegalus* scales have retained many characteristics of the dermal armour of ancient palaeoniscoids[23], and are known to possess a multilayered structure (Fig. 1) of four different organic–inorganic nanocomposite material layers (from outer to inner surface): ganoine, a type of enamel (thickness ~ 10 μm), dentine (thickness ~ 50 μm), isopedine (thickness ~ 40 μm) and a bone basal plate (thickness ~ 300 μm) (ref. 21). Instrumented nanoindentation was used to measure the penetration resistance, as well as elastic and plastic mechanical properties, spatially through the four layers that compose

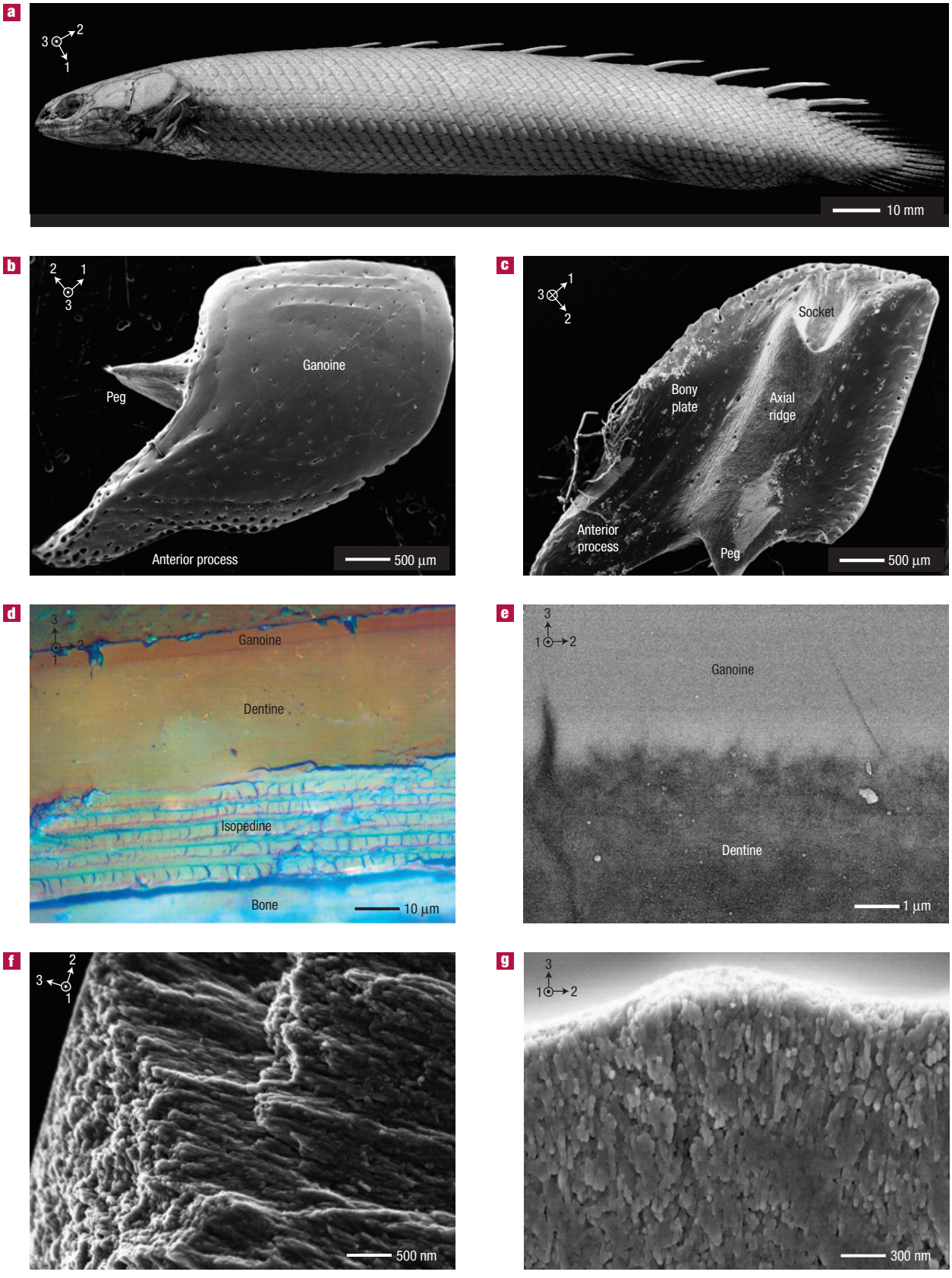

Figure 1 Structure of *Polypterus senegalus* scale. a, *P. senegalus* skeleton[40]. **b**, Scanning electron micrograph (SEM) of outer scale surface. **c**, SEM of the inner scale surface. **d**, Optical micrograph of the cross-section of an individual scale showing four layers; only a fraction of the bony basal plate is visible. **e**, Backscattered electron microscopy image of the cross-section of the ganoine–dentine junction. **f**, SEM image of ganoine nanocrystals. **g**, SEM image of ganoine cross-section.

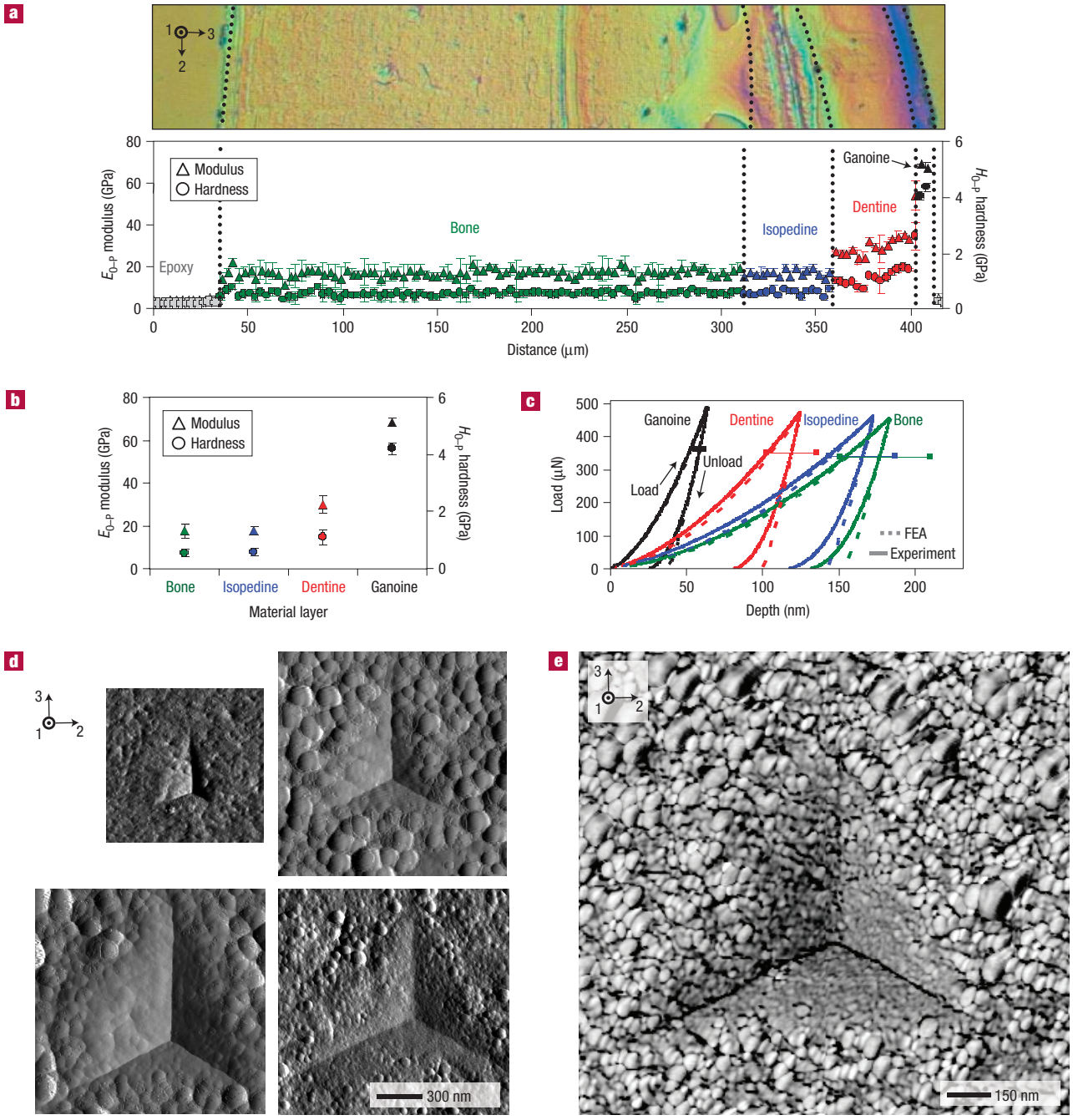

Figure 2 Mechanical properties derived from nanoindentation experiments across the cross-section of the different material layers of an individual *P. senegalus* scale. All data represent an average of three parallel columns of 125 indents each. **a**, 500 μN maximum load; average indentation modulus, E_{0-P}, and hardness, H_{0-P}, both reduced from Oliver–Pharr analysis[24] as a function of distance across the scale cross-section. The vertical error bars represent one standard deviation. 'Epoxy' is epoxy used for embedding. **b**, Average E_{0-P} and H_{0-P} for each of the different layers derived from 500-μN-maximum-load nanoindentation curves. The vertical error bars represent one standard deviation for that particular dataset. **c**, Average nanoindentation load–depth curves for all four material layers. Horizontal error bars represent one experimental standard deviation. **d**, TMAFM amplitude images of the residual indents (500 μN maximum load) on the cross-section of each of the four material layers. Top left to bottom right: ganoine, dentine, isopedine and bone. **e**, TMAFM phase image of the residual indentation (500 μN maximum load) on the isopedine cross-section.

the cross-section of an individual scale from *P. senegalus*. A representative dataset is presented in Fig. 2a; the Oliver–Pharr[24] calculated indentation modulus, E_{O-P}, and hardness, H_{O-P}, both decrease with distance from the outer to the inner surfaces of the scale (from ~62 GPa to ~17 GPa and from ~4.5 GPa to ~0.54 GPa, respectively; Fig. 2b). Each material layer was found to have significantly different mechanical properties compared with the others ($p < 0.05$), except for bone compared with isopedine. The highest average indentation modulus (~62 GPa) and hardness (~4.5 GPa) of the outer ganoine layer is consistent with its

known highly mineralized (<5% organic[25]) non-collagenous structure composed of rodlike, pseudoprismatic crystallites of apatite (Fig. 1f,g)[26]. The collagenous dentine layer has a reduced mineral content compared with ganoine, but is more mineralized than the osseous basal plate[21], consistent with the mechanical property trends observed in Fig. 2a,b (E_{O-P} and $H_{O-P} \sim 29$ GPa and 1.2 GPa, respectively). The third layer, isopedine, consists of a uniform superimposition of orthogonal collagenous layers that form a plywood-like structure and decrease in mineralization with distance towards the inner surface of the scale[27]. The innermost thick basal osseous plate is composed of a succession of vascularized bone lamellae, with the major axis of the collagen fibrils approximately parallel to the scale surface[21]. Besides the spatial organization of their fibres, isopedine and bone also differ in the larger diameter of the isopedine collagen fibrils (~100 nm versus ~20 nm, respectively) and in the thickness of its sublayers (~3–10 μm versus <1 μm, respectively)[28]. Averaged E_{O-P} and H_{O-P} for bone were found to be slightly less than isopedine (Fig. 2b), but this difference was not statistically significant ($p > 0.05$). Multiple cross-sectional indents were taken on an individual scale, on different scales from the same animal and on scales from a number of different animals, and the trends described above were consistently obtained.

The gradation in material properties was calculated as the slope of data such as that shown in Fig. 2a. An approximately negative linear gradation (from the outer to inner surface) in both E_{O-P} and H_{O-P} exists within the outer ganoine ($-1.16\,GPa\,\mu m^{-1}$ and $-0.2\,GPa\,\mu m^{-1}$, respectively) and underlying dentine ($-0.23\,GPa\,\mu m^{-1}$ and $-0.015\,GPa\,\mu m^{-1}$, respectively) layers. Isopedine and bone were found to show no detectable gradation. The ganoine–dentine and dentine–isopedine junctions (Fig. 2a, dotted lines) possessed a steep gradation relative to their neighbouring layers. For the ganoine–dentine junction the gradients in E_{O-P} and H_{O-P} were found to be $5.9\,GPa\,\mu m^{-1}$ and $-0.44\,GPa\,\mu m^{-1}$, respectively. For the dentine–isopedine junction, the gradients in E_{O-P} and H_{O-P} were found to be $-3.2\,GPa\,\mu m^{-1}$ and $-0.1\,GPa\,\mu m^{-1}$, respectively. The ganoine–dentine junction was observed to show an exceedingly sharp (<500 nm) and corrugated junction between the layers (Fig. 1e).

The averaged experimental load–depth data for each layer were fitted to an isotropic, elastic–perfectly plastic finite element analysis (FEA) computational model (Fig. 2c), which represents the three-dimensional Berkovich indenter geometry as two dimensional, axisymmetric, conical-like and rigid. A finite residual depth observed experimentally after unloading (Fig. 2c) and residual impressions directly imaged by tapping mode atomic force microscopy (TMAFM, Fig. 2d,e) confirm the plastic nature of indentation. In these simulations, the indentation modulus, E, and the yield stress, σ_Y, were determined by a best fit to the averaged loading and unloading experimental data (Fig. 2c), with the indentation modulus calculated from the FEA-predicted unloading slope[24] matched to the experimentally calculated average E_{O-P} (Fig. 2b). Figure 2c shows good agreement between the FEA predictions and the experimental data, giving σ_Y values of 2,000, 400, 215 and 180 MPa for the ganoine, dentine, isopedine and bone, respectively. An extensive parametric study showed that the inclusion of post yield strain hardening (linear isotropic hardening, linear kinematic hardening and Ramberg–Osgood isotropic hardening) in the simulations had a minimal effect in providing an improved prediction of the nanoindentation load–depth data and the estimated yield stress. All material layers were observed to undergo mechanical hysteresis (Fig. 2c), and energy dissipation (calculated as the area of the average indentation loading–unloading cycle) increased with distance from the outer surface of the scale inward from ganoine ~5.98 pJ to bone ~23.79 pJ.

The role of the local multilayered and graded micromechanical properties in the larger-length-scale biomechanical microindentation of the entire *P. senegalus* scale was explored by constructing two axisymmetric, two-dimensional FEA models (Fig. 3a). The first, 'discrete', model (Fig. 3a) was composed of the four material layers with thicknesses corresponding to their experimentally measured values (Fig. 1d), where each layer was assumed to possess isotropic, elastic–perfectly plastic constitutive behaviour with E and σ_Y taken as those reduced from FEA predictions of the averaged load–depth data in Fig. 2c. The second, 'gradient', model (Fig. 3a) was also composed of the four material layers with thicknesses corresponding to their experimentally measured values (Fig. 1d) and assumed isotropic elastic–perfectly plastic material behaviour, but incorporated linear gradients in E (scaled by the measured E_{O-P} gradient values) and σ_Y (scaled with the measured H_{O-P} gradient values) within the ganoine and dentine layers, as well as the ganoine–dentine and dentine–isopedine junctions. The predictions of these two multilayered models were compared with three simulations of a single homogeneous elastic–perfectly plastic layer of material with a thickness equivalent to that of the entire scale (~400 μm): ganoine, dentine and bone. Virtual microindentation experiments were then carried out using an axisymmetric, conical-like, rigid indenter (emulating an axisymmetric equivalent Vicker's microhardness tip, end radius ~3.7 μm, conical angle ~70.3°) (Fig. 3b). The two multilayered model predictions both tracked the ganoine load–depth curve up to ~0.10 N, and then at increasing penetrations fell in between the all ganoine and all dentine simulations (Fig. 3b). For the multilayered simulations, at a maximum load of 0.5 N, the indenter had penetrated ~45% of the way into the ganoine layer (Fig. 3b). There was minimal difference observed in the load–depth behaviour for the discrete and gradient models, indicating that the overall microlayering (not the gradients) provides the effective 'macroscopic' effective mechanical load–depth resistance (which does not suggest that gradients do not play a role in penetration resistance, discussed further below).

The 'effective' behaviour of the microlayered structures was further examined by reducing each load–depth behaviour to an effective O–P modulus, effective microhardness and energy dissipation. Interestingly, a load-dependent effective modulus and microhardness are predicted for the multilayered models, which is not the case for the homogeneous systems (Fig. 3c,d). The effective modulus for these two models is seen to decrease nonlinearly from close to that of all ganoine at small maximum loads to values slightly below that of all dentine by a maximum load of 1 N (corresponding to a penetration depth of ~5.5–5.7 μm, Fig. 3c). Hence, the underlying micromechanics of the multilayered structure directly govern the effective 'macroscopic' indentation modulus, where the indenter increasingly 'senses' the more compliant dentine layer as the indentation load is increased. For the multilayered simulations, the effective microhardness is also predicted to decrease sigmoidally between values corresponding to all ganoine (at small maximum loads < 0.1 N) and all dentine (1 N maximum load, corresponding to a penetration depth of ~5.5–5.7 μm, Fig. 3d). The multilayer microhardness predictions were compared with experimentally measured Vickers hardness (measured using TMAFM and optical microscopy) on an individual *P. senegalus* scale and the magnitude and load dependency were accurately captured (Fig. 3d). The effective energy dissipation of the microlayered models were found to increase nonlinearly with maximum load (Fig. 3e) and fell in between the all-ganoine and all-dentine curves.

Figure 4 shows the stress contours and plastic equivalent strain after unloading (maximum load of 1 N) for the simulated microindentation multilayer models as compared with that of the

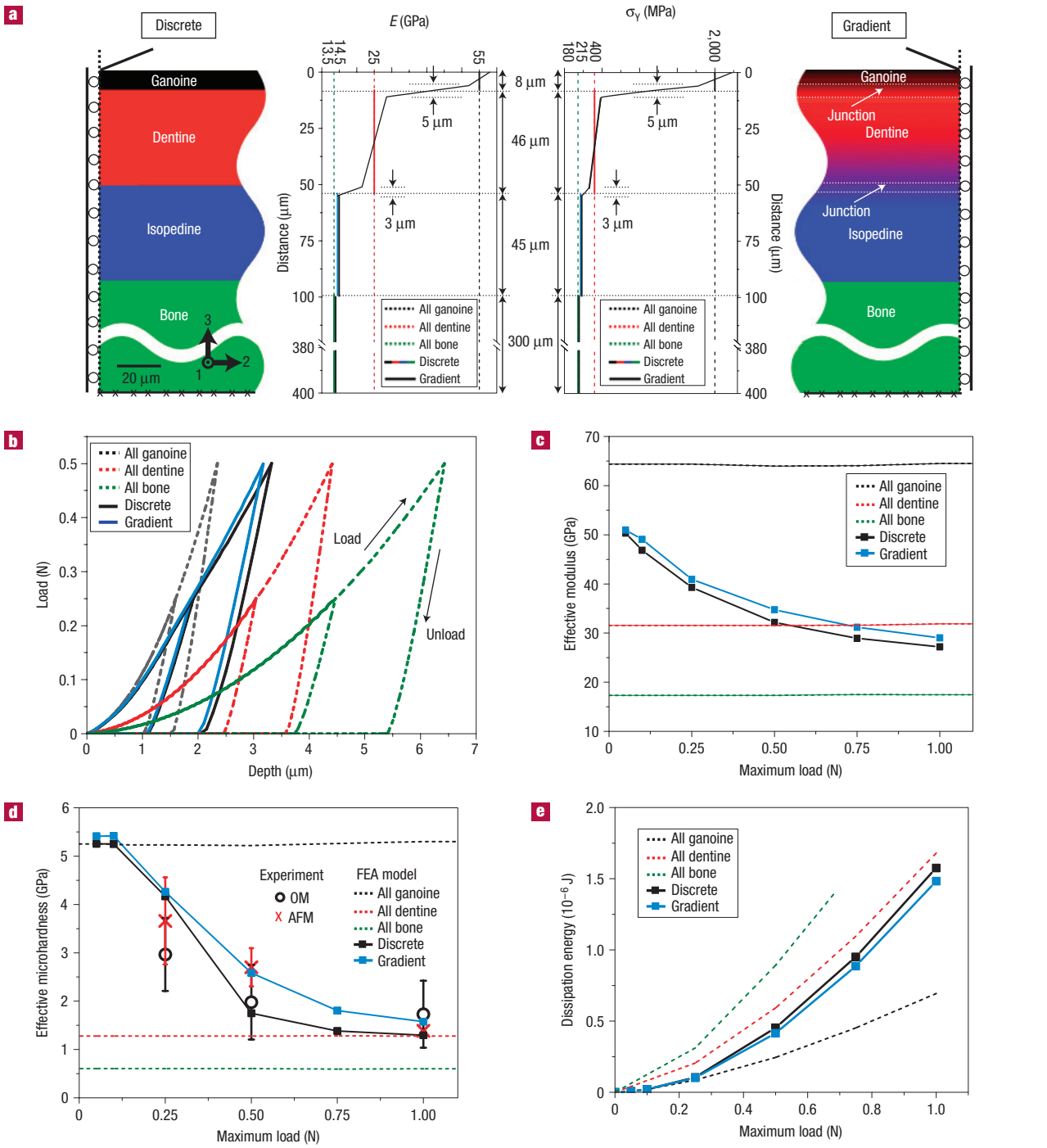

Figure 3 Predictions of effective microindentation mechanical properties of *P. senegalus* scale via multilayered FEA simulations. **a**, Multilayered structures of discrete (left) and gradient (right) models with their corresponding elastic modulus and yield strength distributions (centre). **b**, Simulated microindentation load-versus-depth curves. **c**, Simulated effective indentation modulus. **d**, Simulated effective microhardness and experimentally measured values (OM, optical microscopy; AFM, atomic force microscopy). **e**, Simulated effective energy dissipation.

all-ganoine material. The gradient junction is observed to provide a transitional region for stress redistribution between layers of differing materials (Fig. 4c), as opposed to the abrupt changes observed in the discrete model (Fig. 4b). Such smoother stress gradients are expected to mitigate interface failure and increase interfacial toughness, thereby providing increased penetration resistance. Although the discrete and gradient multilayered systems achieve similar macroscopic effective indentation modulus and microhardness, the gradient case micromechanically achieves more gradual stress redistribution, providing robustness to interfacial failures. The plastic equivalent strain contours reveal the greater depths and greater area of plastic straining for the multilayer

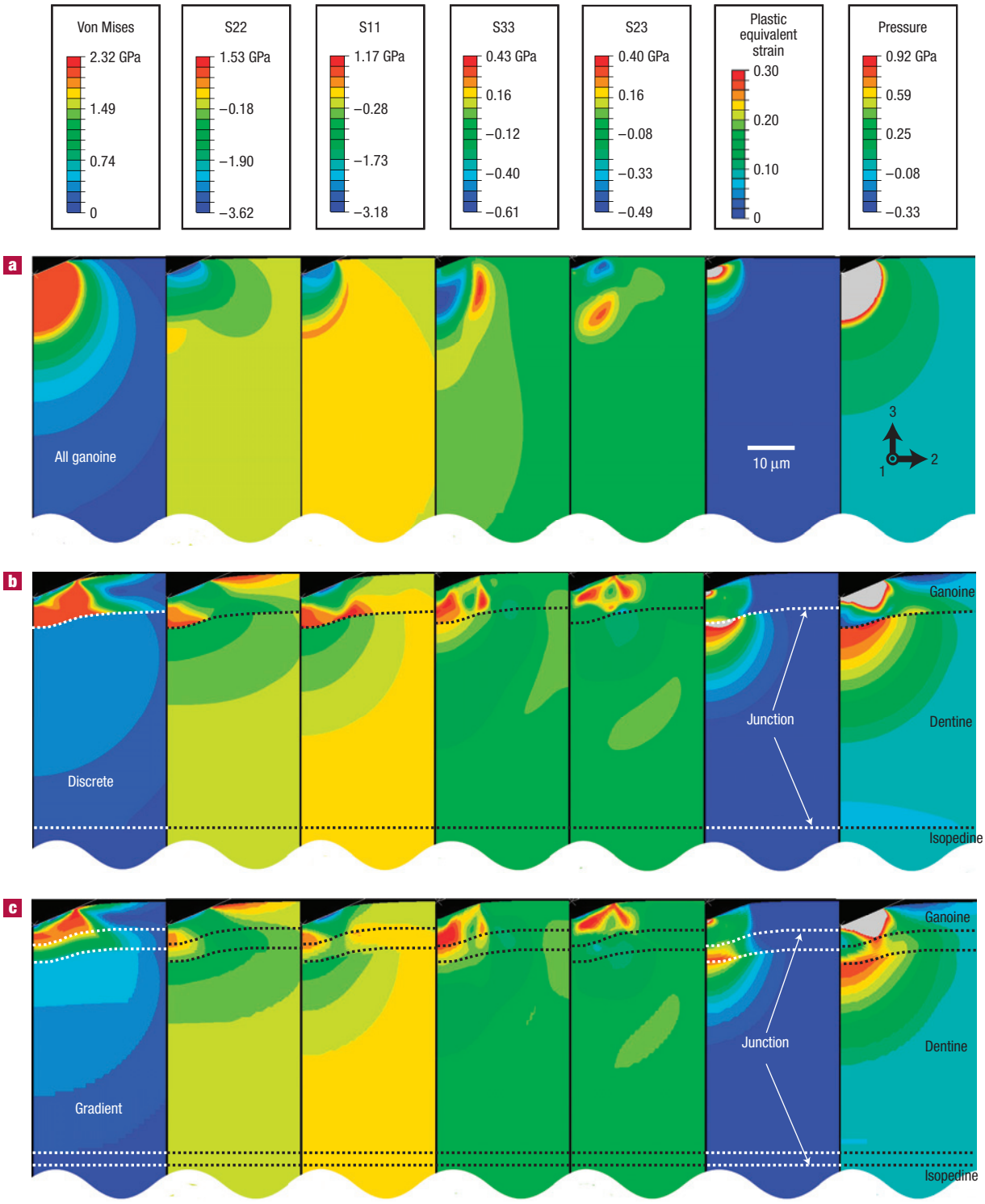

Figure 4 Simulation contours of stress, plastic strain and pressure fields of a *P. senegalus* scale via multilayered FEA simulations. a–c, FEA predictions of von Mises stress field, S22 (normal stress on the plane perpendicular to the 2 axis), S11 (normal stress on the plane perpendicular to the 1 axis) and pressure at a maximum depth when fully loaded, and S23 (shear stress on the plane perpendicular to the 3 axis acting in the 2 direction), S33 (normal stress on the plane perpendicular to the 3 axis) and plastic equivalent strain after fully unloaded for three models: all ganoine (**a**), discrete (**b**) and gradient (**c**) models for 1-N-maximum-load indentation.

system compared with the all-ganoine model, due to the increased plastic strain of the underlying dentine, which possesses a lower σ_Y compared with ganoine; this correlates with the greater dissipation seen in the load–depth curves (Fig. 2b,e). The simulations also show that the magnitude of the plastic strain in the ganoine layer of the multilayered system is lower than that experienced in the

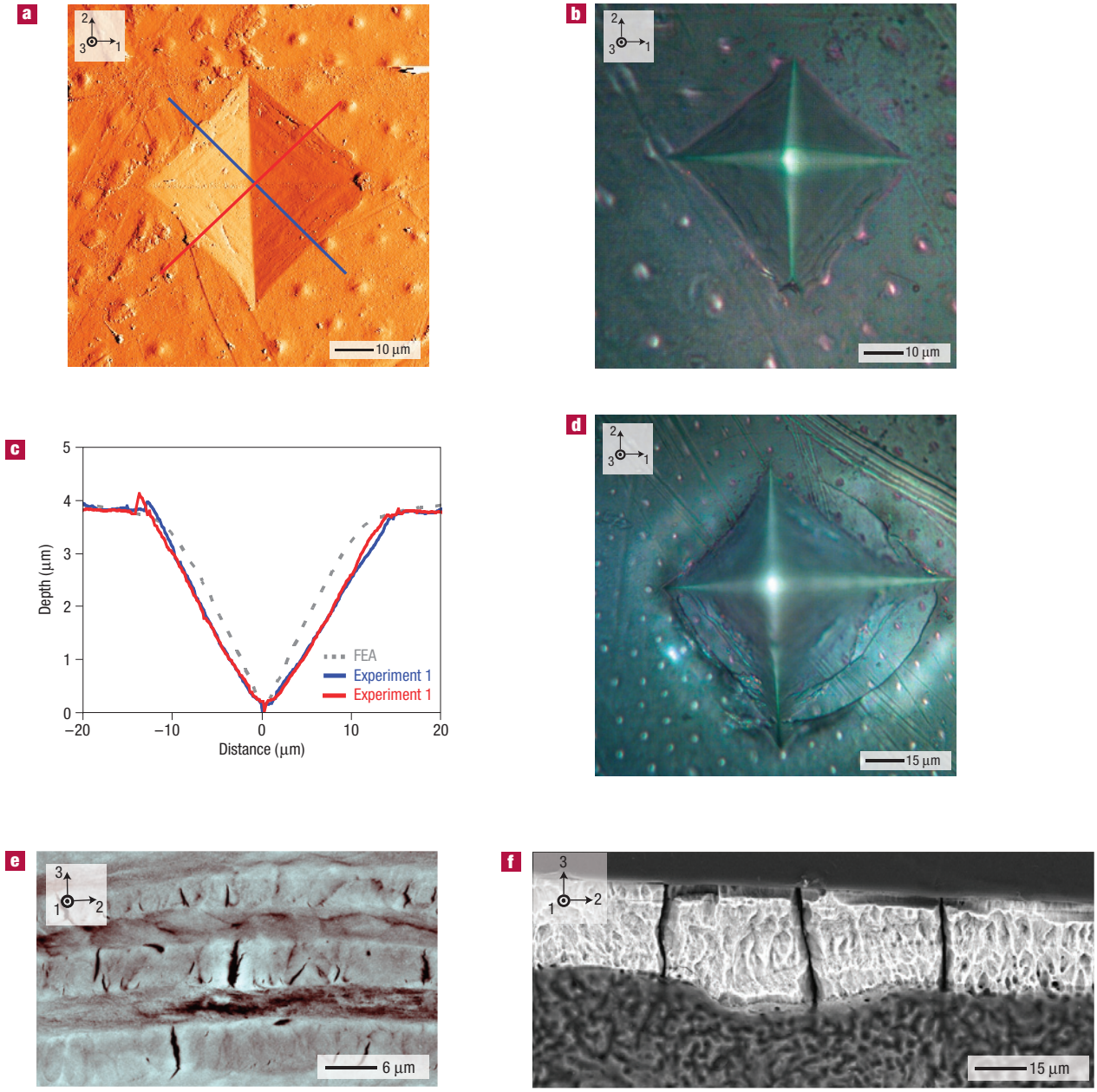

Figure 5 Topographic profiles, residual impressions of microindentation and fracture of an individual *P. senegalus* scale. a, TMAFM amplitude image of a 1-N-maximum-load microindentation. **b**, Optical micrograph of a 1-N-maximum-load microindentation. **c**, FEA prediction of the residual depth topography obtained from the gradient multilayer simulation and experimental height profiles from TMAFM images (Fig. 5a) for 1-N-maximum-load microindentation. **d**, Optical micrograph of a 2 N microindentation showing circumferential cracks. **e**, SEM of cross-section of isopedine layers. **f**, Backscattered electron micrograph of cross-section of ganoine and dentine layers.

all-ganoine system, even though the overall depth of penetration in the multilayer (5.46–5.72 μm) is more than twice that of the all-ganoine system (3.63 μm), a direct result of the dentine deformation accommodating the imposed penetration depth.

The 1 N maximum load is appropriate to estimate a brittle-failure condition for the ganoine because 1 N microhardness experiments were found to circumferentially crack in some cases and only plastically strain in other cases (Fig. 5)—indicating that the 1 N case is at the border of meeting crack initiation conditions. Contours of the radial stress, S22 (Fig. 4), reveal elevated tensile surface values (1.66 GPa) at the perimeter of the contact area (in the same region where the circumferential cracks are found), suggesting a maximum-normal-brittle-stress failure condition of 1.66 GPa. The values are lower and the regions of elevated stress are smaller in the gradient case than the discrete case, indicating an important smoothing role of the gradient in reducing the surface stresses. A second prominent surface failure condition is often radial cracks, which were not observed in these microhardness experiments; this is consistent with the simulation results, which show the surface circumferential stress values, S11, that would

be needed to initiate radial cracks to be <S22. (Parametric computational studies on the effect of the ganoine thickness show that the experimentally observed values (5–20 μm) yield S22 > S11, which promotes circumferential cracking (observed experimentally Fig. 5d), which is highly advantageous because it locally confines the deformation at the indentation site. For a thicker or thinner ganoine layer, S11 remains large, which promotes undesirable radial cracking, which can lead to catastrophic failure of the layer.) As seen in other multilayer systems[29], the interfacial normal and shear stresses were found to be severe on unloading (S33, S23, Fig. 4). The stresses are found to be similar for the discrete and gradient systems with the expectation of a peak shear stress present on the interface of the discrete system, which is absent from the gradient system. Excellent agreement between simulation and experiment was also demonstrated in comparison of the experimentally measured residual topography (Fig. 5). The 0.5 N cases deformed in an elastic–plastic manner with no cracks in most cases (~9 of 10 indents; Fig. 5a,b). For 1 N, ~50% of the samples showed circumferential cracking. Circumferential cracks were observed in all of the 2.0 N cases (Fig. 5d).

Although mineralized dermal fish scales serve many functional roles simultaneously[5–7], we limit our discussion here to protective biomechanical aspects[4]. The primary predators of *P. senegalus* are known to be its own species or its carnivorous vertebrate relatives[4], and biting takes place during territorial fighting[22] and feeding[30]. In ancient times, many large invertebrate predators existed. For example, the carnivorous eurypterid (thought to be a predator of the armoured ostracoderms) was a giant arthropod that possessed biting mouth parts, grasping jaws, claws, spines and a spiked tail[4]. Additionally, it has been suggested that the placoderm *Dukleosteus terelli* possessed a bite force large enough to puncture through the mineralized exoskeleton of its prey, to consume the flesh underneath[8]. Mechanically, such predatory attacks would represent a dynamic (for *P. senegalus*[31]) penetrating load (approximated by the multilayered indentation simulations), which involves a spatially localized, multiaxial and largely compressive stress field. *P. senegalus* shows a multilayered scale design over a micrometre-sized length scale, suggesting that the purpose of this design is for resistance to mechanical loads and deformations existing over these small length scales as well. For example, the teeth of a similar-sized *P. senegalus* were measured to possess an end-radius of 14.7±8.8 μm, ranging from ~3.0 to ~44.0 μm. A finite-element geometric representation of the teeth of *P. senegalus* was created and FEA indentation simulations carried out using these meshes (which are much larger than the standard Vickers nanoindenter, end radius ~3.7 μm, reported in the current manuscript) using the multilayered scale model. All of the trends and conclusions of the current paper remained the same using this fish-tooth-representation indentation. Hence, the micrometre length scale and indentation mode of deformation within individual scales are physiologically important with regard to mitigating penetration and facilitating protection, working in conjunction with the larger, multiscale structure of the armour, which enables a significant amount of biomechanical flexibility and manoeuvrability of the entire fish body[32].

In conclusion, here we report on the fascinating, complex and multiscale materials design principles of ancient fish armour in the context of its specific primary environmental threat (penetrating biting attacks) and mechanically protective function. One overarching mechanical design strategy is the juxtaposition of multiple distinct reinforcing layers, each of which has its own unique deformation and energy dissipation mechanisms. As the stiff ganoine transfers load through the ganoine–dentine junction, the underlying softer, more compliant dentine layer dissipates energy via plasticity (at high enough loads). The ganoine thickness was selected (1) to simultaneously access the advantageous mechanical properties of the ganoine (hardness, stiffness) and underlying dentine (energy dissipation), (2) to reduce weight while maintaining the required mechanical properties and (3) to promote the advantageous circumferential cracking mechanism (S22 > S11), rather than disadvantageous radial cracking. The material layer sequence is also critical; for example, reversing the ganoine and dentine layers in a virtual microindentation leads to magnified interfacial tensile normal and shear stresses, promoting delamination (data not shown). The presence of the additional isopedine stratified layer with its plywood-like structure can serve as a second line of defence for deeper penetrations, preventing catastrophic crack propagation and increasing energy dissipation and fracture toughness. Microcracking was observed to be confined within the sublayers of the isopedine (Fig. 5e), where each layer has cracks running in approximately orthogonal directions (consistent with the known structure) but arrested at the edge of each sublayer. The underlying bone acts as the base skeletal physical support structure for normal physiological loading conditions, where plastic deformation (if forced beyond the elastic limit via a traumatic event) takes place via mechanisms such as nanogranular friction[33], collagen fibril shear[34] and denaturation[35], crack initiation–propagation[36], intraorganic extensibility and sacrificial bond rupture[14]. The quad-layered design of *P. senegalus* scales enables weight reduction of up to ~20%, compared with a bilayer of ganoine and dentine of the same thickness, with minimal degradation of effective mechanical properties (that is, microhardness, modulus, energy dissipation). Additionally, we have observed that the ganoine–dentine junction in *P. senegalus* scales is able to arrest cracks (Fig. 5f), as in mammalian teeth[37]. Localized internal fractures and detachment of pieces of the ganoine layer are seen, whereas the ganoine–dentine junction consistently remains intact (Fig. 5f), which may be a sacrificial mechanism. The junctions between material layers are clearly 'functionally graded', that is, they possess a gradual spatial change in properties motivated by the performance requirements and are able to promote load transfer and stress redistribution, thereby suppressing plasticity, arresting cracks, improving adhesion and preventing delamination between dissimilar material layers[38]. Last, the corrugated junction between the layers is expected to lead to spatially heterogeneous stresses and a higher net interfacial compression, also resisting delamination[39]. Such multiscale materials principles may be incorporated into the design of improved engineered biomimetic structural materials[20].

METHODS

EXPERIMENTAL DETAILS

Anaesthesia of a living *P. senegalus* was induced by approximately 15 min of immersion in a buffered 0.03% (by weight) solution of tricaine methane sulphonate (MS222). Surgery was carried out and a row of 3–5 scales was removed during which anaesthesia was maintained by a 0.015% solution of MS222. After the surgery, the water of the tank was treated with tetracycline tablets for two weeks to prevent infection and within two months the removed scales were regenerated. All experiments were performed in accordance with federal guidelines and regulations and approved by the MIT Committee on Animal Care (Protocol 0707-056-10). MIT has an Animal Welfare Assurance on file with the Office for Laboratory Animal Welfare (Assurance number A-3125-01).

Freshly extracted scales from a living adult *P. senegalus* were embedded in a room-temperature curing epoxy (Loctite Fixmaster Poxy-Pak 81120) and sectioned using a diamond-impregnated annular wafering saw (Buehler Isomet 5000) at 800–900 r.p.m. The samples were polished on a polishing wheel (South Bay Technology, Model 920) with 15 μm, 6 μm and 1 μm silica nanoparticles on a soft pad, and again with 50 nm silica nanoparticles on a cloth pad in distilled water. Samples were stored in phosphate-buffered saline solution. Samples

were imaged in a JEOL JSM-6060 SEM or a JEOL JSM-6700F field emission SEM. Backscattered electron microscope images were taken with a JEOL JSM-6700F. Optical microscopy images were taken with a Nikon Eclipse L150. Nanoindentation experiments were conducted in ambient conditions using a Hysitron Triboindenter using a Berkovich diamond probe tip, following our previously reported methods[15,17]. Artifacts due to surface roughness, surface slope, residual indent overlap and so on were carefully avoided, as described in detail previously[15,17]. Unpaired Student t-tests were carried out to evaluate whether various datasets were statistically different from one another, using $p < 0.05$ as the minimum criterion. Vickers microhardness experiments were conducted in ambient conditions. The probe-tip end radius was measured using TMAFM ($\sim$3.7 μm). TMAFM imaging was carried out with a Multimode SPM IV (Veeco) and Si cantilevers (Veeco, V-shaped, square pyramidal probe tip, k (nominal spring constant) $\sim 0.40\ \mathrm{N\,m^{-1}}$; R_{tip} (nominal probe-tip end radius of curvature) $\sim$ 10 nm).

FINITE ELEMENT ANALYSIS

A nonlinear FEA nanoindentation model was used, which approximated the three-dimensional Berkovich nanoindentation experiments using a two-dimensional, conical-like axisymmetric indenter. The accuracy of the two-dimensional axisymmetric approximation was assessed by comparison with fully three-dimensional simulation results; the modulus and yield stress values obtained in the two-dimensional simulations differed from those from three dimensions by less than 2–3% (a range within any experimental comparison significance). The indenter geometry was chosen to correspond to the experimentally determined indenter cross-sectional tip-area function. The indenter tip was modelled as rigid. The indented samples were modelled as isotropic, elastic–perfectly plastic using four-node bilinear axisymmetric quadrilateral elements (CAX4R in ABAQUS element library). Large-deformation theory and frictionless contact between the indenter and material were assumed. Full three-dimensional nanoindentation simulations were also conducted on samples with two layers oriented normal to the surface, simulating several indentations with each indentation progressively closer to the layer–layer interface to assess the role of any constraint of a neighbouring layer on the indentation load–depth behaviour. FEA models of microindentation followed a similar methodology to the axisymmetric nanoindentation simulations. The indenter was taken to be rigid, with a conical tip geometry, emulating a Vickers microhardness tip with a radius of 3.7 μm (measured by AFM). Mesh convergence studies were used to assess the needed mesh for accurate solutions to the load–depth and stress contours.

Received 14 January 2008; accepted 23 June 2008; published 27 July 2008.

References

1. Hoedeman, J. J. *Naturalists Guide to Fresh Water Aquarium Fish* (Sterling Publishing Co., Oak Tree Press Co., New York, London, and Sydney, 1974).
2. Colbert, E. H. *Evolution of the Vertebrates: A History of Backboned Animals Through Time* (Wiley, New York, 1955).
3. Miller, H. *The Cruise of the Betsy or Summer Holiday in the Hebrides with Rambles of a Geologist or Ten Thousand Miles of Fossiliferous Deposits of Scotland* (Gould and Lincoln, Boston, 1857).
4. Romer, A. S. Eurypterid influence on vertebrate history. *Science* **78**, 114–117 (1933).
5. Ørvig, T. in *Proc. 4th Nobel Symp.* (ed. Ørvig, T.) 373–397 (Almqvist and Wiskell, Stockholm, 1968).
6. Long, J. H. & Nipper, K. S. The importance of body stiffness in undulatory propulsion. *Am. Zool.* **36**, 678–694 (1996).
7. Raschi, W. & Tabit, C. Functional aspects of placoid scales: A review and update. *Aust. J. Mar. Freshw. Res.* **43**, 123–147 (1992).
8. Anderson, P. S. L. & Westneat, M. W. Feeding mechanics and bite force modelling of the skull of *Dunkleosteus terrelli*, an ancient apex predator. *Biol. Lett.* **22**, 76–79 (2007).
9. Arciszewski, T. & Cornell, J. in *Bio-Inspiration: Learning Creative Design Principia* (ed. Smith, I. F. C.) (Springer, Berlin, 2006).
10. Weiner, S. & Addadi, L. Design strategies in mineralized biological materials. *J. Mater. Chem.* **7**, 689–702 (1997).
11. Gao, H., Ji, B., Jager, I. L., Arzt, E. & Fratzl, P. Materials become insensitive to flaws at nanoscale: Lessons from nature. *Proc. Natl Acad. Sci. USA* **100**, 5597–5600 (2003).
12. Buehler, M. J. Molecular nanomechanics of nascent bone: Fibrillar toughening by mineralization. *Nanotechnology* **18**, 1–9 (2007).
13. Currey, J. D. The design of mineralised hard tissues for their mechanical functions. *J. Exp. Biol.* **202**, 3285–3294 (1999).
14. Fantner, G. E. *et al.* Sacrificial bonds and hidden length dissipate energy as mineralized fibrils separate during bone fracture. *Nature Mater.* **4**, 612–616 (2005).
15. Tai, K., Dao, M., Suresh, S., Palazoglu, A. & Ortiz, C. Nanoscale heterogeneity promotes energy dissipation in bone. *Nature Mater.* **6**, 454–462 (2007).
16. Balooch, G. *et al.* Evaluation of a new modulus mapping technique to investigate microstructural features of human teeth. *J. Biomech.* **37**, 1223–1232 (2004).
17. Bruet, B. J. F. *et al.* Nanoscale morphology and indentation of individual nacre tablets from the gastropod mollusc *Trochus niloticus*. *J. Mater. Res.* **20**, 2400–2419 (2005).
18. Raabe, D., Sachs, C. & Romano, P. The crustacean exoskeleton as an example of a structurally and mechanically graded biological nanocomposite material. *Acta Mater.* **53**, 4281–4292 (2005).
19. Barbakadze, N., Enders, S., Gorb, S. & Arzt, E. Local mechanical properties of the head articulation cuticle in the beetle *Pachnoda marginata* (Coleoptera, Scarabaeidae). *J. Exp. Biol.* **209**, 722–730 (2006).
20. Ortiz, C. & Boyce, M. C. Bioinspired structural materials. *Science* **319**, 1053–1054 (2008).
21. Daget, J., Gayet, M., Meunier, F. J. & Sire, J.-Y. Major discoveries on the dermal skeleton of fossil and recent polypteriforms: A review. *Fish Fisheries* **2**, 113–124 (2001).
22. Kodera, H. *et al. Jurassic Fishes: Selection, Care, Behavior* (T. F. H. Publications, New Jersey, 1994).
23. Carroll, R. L. *Vertebrate Paleontology and Evolution* (W. H. Freeman and Company, New York, 1988).
24. Oliver, W. C. & Pharr, G. M. An improved technique for determining hardness and elastic modulus using load and displacement sensing indentation experiments. *J. Mater. Res.* **7**, 1564–1583 (1992).
25. Ørvig, T. in *Structural and Chemical Organization of Teeth* (ed. Miles, A. E.) Ch. 2, 45–110 (Academic, New York, 1967).
26. Meunier, F. J. Recherches histologiques sur le squelette dermique des Polypteridae. *Archives de Zoologie Expérimentale et Générale* **122**, 279–295 (1980).
27. Meunier, F. J. Os cellulaire, os acellulaire et tissus dérivés chez les Ostéichthyens: Les phénomènes de l'acellularisation et de la perte de minéralisation. *L'Année Biologique* **26**, 201–233 (1987).
28. Sire, J.-Y. From ganoid to elasmoid scales in the Actinopterygian fishes. *Neth. J. Zool.* **40**, 75–92 (1990).
29. Jayachandran, R., Boyce, M. C. & Argon, A. S. Design of multilayer polymeric coatings for indentation resistance. *J. Comput.-Aided Mater. Design* **2**, 151–166 (1995).
30. Markey, M. J., Main, R. P. & Marshall, C. R. In vivo cranial suture function and suture morphology in the extant fish Polypterus: Implications for inferring skull function in living and fossil fish. *J. Exp. Biol.* **209**, 2085–2102 (2006).
31. Lauder, G. V. Evolution of the feeding mechanism in primitive actinopterygian fishes; a functional anatomical analysis of Polypterus, Lepisosteus, and Amia. *J. Morphol.* **163**, 283–317 (1980).
32. Gemballa, S. & Bartsch, P. Architecture of the integument in lower Teleostomes: Functional morphology and evolutionary implications. *J. Morphol.* **253**, 290–309 (2002).
33. Tai, K., Ulm, F.-J. & Ortiz, C. Nanogranular origins of the strength of bone. *Nano Lett.* **6**, 2520–2525 (2006).
34. Gupta, H. S. *et al.* Nanoscale deformation mechanisms in bone. *Nano Lett.* **5**, 2108–2111 (2005).
35. Tai, K., Qi, H.-J. & Ortiz, C. Effect of mineral content on the nanoindentation properties and nanoscale deformation mechanisms of bovine tibial cortical bone. *J. Mater. Sci.: Mater. Med.* **16**, 947–959 (2005).
36. Nalla, R. K., Kinney, J. H. & Ritchie, R. O. Mechanistic fracture criteria for the failure of human cortical bone. *Nature Mater.* **2**, 164–168 (2003).
37. Imbeni, V., Kruzic, J. J., Marshall, G. W. & Ritchie, R. O. The dentin–enamel junction and the fracture of human teeth. *Nature Mater.* **4**, 229–232 (2005).
38. Suresh, S. Graded materials for resistance to contact deformation and damage. *Science* **292**, 2447–2451 (2001).
39. Shimizu, D. & Macho, G. A. Functional significance of the microstructural detail of the primate dentino-enamel junction: A possible example of exaption. *J. Human Evolut.* **52**, 103–111 (2007).
40. Humphries, J. *Polypterus senegalus*, online digital morphology. Accessed June 1, 2007 at <http://digimorph.Org/specimens/polypterus_senegalus/whole/> (Michigan Museum of Zoology) (ummz 195008). (2003).

Acknowledgements

The authors thank the MIT Department of Materials Science and Engineering Nanomechanical Testing Facility, the National Science Foundation MIT Center for Materials Science and Engineering, the Centre de Recherche de la Matière Condensée et des Nanosciences (CRMC-N) at Université de Marseille-Luminy, France, the MIT International Science and Technology Initiatives—France Seed Fund and the US Army through the MIT Institute for Soldier Nanotechnologies (contract number DAAD-19-02-D0002), as well as R. Jensen and T. Weerasooriya from the US Army Research Laboratory and T. Imholt from Raytheon for discussions. The content does not necessarily reflect the position of the government and no official endorsement should be inferred. The authors would also like to thank E. Chen, J. H. Choi, J. Kim, J. Y. Mao, M. D. Mascaro and E. R. Pfeiffer for assisting with initial sample preparation and preliminary data, A. Baronnet for assistance with electron microscopy and G. Lauder (Harvard University) for carrying out the scale-removal surgery.

Author information

Reprints and permission information is available online at http://npg.nature.com/reprintsandpermissions. Correspondence and requests for materials should be addressed to C.O.